Letter

Topological excitonic corner states and nodal phase in bilayer quantum spin Hall insulators

Zheng-Rong Liu,[1] Lun-Hui Hu,[2] Chui-Zhen Chen,[3] Bin Zhou,[1] and Dong-Hui Xu[1,*]

[1]*Department of Physics, Hubei University, Wuhan 430062, China*

[2]*Department of Physics, the Pennsylvania State University, University Park, Pennsylvania 16802, USA*

[3]*Institute for Advanced Study and School of Physical Science and Technology, Soochow University, Suzhou 215006, China*

(Received 7 January 2021; revised 5 May 2021; accepted 12 May 2021; published 21 May 2021)

Interaction induced topological states remain one of the most fascinating phenomena in condensed matter physics. The exciton condensate has recently sparked renewed interest due to the discovery of new candidate materials and its driving force to realize exotic topological states. In this work, we explore the exciton order induced high-order topology in the bilayer quantum spin Hall insulators and find that the topological excitonic corner states can be realized by tuning the gate and magnetic field. When an in-plane Zeeman field is applied to the system, two or four excitonic boundary-obstructed corner states emerge in the bilayer system for distinct possible *s*-wave excitonic pairings. Besides, we also find a two-dimensional excitonic Weyl nodal phase, which supports flat band edge states connecting the bulk Weyl nodes.

DOI: 10.1103/PhysRevB.103.L201115

Introduction. Excitonic insulator [1–4], predicted in the 1960s, is an unconventional insulating state formed by the condensation of excitons (bound electron-hole pairs) stemming from the Coulomb interaction between electrons and holes in the conduction and valence bands, respectively. An excitonic insulator is analogous to a Bardeen-Cooper-Schrieffer superconductor that results from the condensation of electron Cooper pairs developed near the Fermi surface. Candidate materials for excitonic insulators previously studied include quantum well bilayers [5], quantum Hall bilayers [6,7], Ta_2NiSe_5 [8–13], and $1T$-$TiSe_2$ [14–17]. After the discovery of topological insulators, excitonic insulators with topologically nontrivial properties have been investigated intensively [18–33]. Particularly, a few representative topological exciton condensates, including the time-reversal invariant *s*-wave topological exciton condensate and the time-reversal breaking topological exciton condensate with *p*-wave pairing, have been predicted in HgTe/CdTe [23] and InAs/GaSb [24] quantum wells, respectively. Importantly, the evidence for the existence of a topological excitonic insulator state has been reported experimentally in InAs/GaSb quantum wells [34,35].

Recently, the concept of topological insulators was generalized, and a novel topological phase of matter dubbed higher-order topological insulator [36–42] was established. Compared to the well-known topological insulators, higher-order topological insulators exhibit an unusual form of bulk-boundary correspondence. For instance, a second-order topological insulator in two dimensions exhibits topological gapless boundary states at its zero-dimensional boundary corners, in contrast to a conventional two-dimensional (2D) first-order topological insulator which features topologically protected gapless states at its one-dimensional edge. So far, higher-order topology has been explored in various physical systems [43–94], and particularly Majorana zero-energy corner modes [64–66] were found in superconducting systems. Yet, the topological exciton condensates known to date belong to the first-order topological phases, and the study of higher-order topology in exciton condensates is still lacking. Given the similarity of excitonic insulators to superconductors, it is highly desirable to explore higher-order topology of exciton condensates in a realistic system.

In this work, we demonstrate that topological corner states, which are considered as a smoking-gun signature for 2D second-order topological insulators, can be realized in the bilayer quantum spin Hall insulators with *s*-wave interlayer excitonic pairings. The bilayer quantum spin Hall insulators can be constructed by two coupled HgTe/CdTe quantum wells [95] shown in Fig. 1, where the Dirac mass can be tuned by varying the thickness of the central HgTe layers in the quantum wells. For the bilayer system with the negative Dirac mass, four topological excitonic corner states (ECs) are generated by applying an in-plane Zeeman field. By making use of the $\mathbf{k}\cdot\mathbf{p}$ edge theory, we found that ECs originate from the edge mass domain walls formed by the interplay of the excitonic order and the Zeeman field. In the case of the positive Dirac mass, however, only two topological ECs emerge. In addition, we show that an intriguing 2D excitonic nodal phase, which supports flat band edge states connecting the bulk Weyl nodes, could also be realized in this system. Our study suggests that bilayer quantum spin Hall insulators can serve as a platform to host excitonic higher-order topological insulating and nodal phases.

Excitonic corner states for the negative Dirac mass. We report that a high-order topological excitonic insulator can be achieved in the bilayer quantum spin Hall insulators by tuning the bias voltage and in-plane Zeeman field. The low-energy effective Hamiltonian of the gated bilayer quantum spin Hall insulators with an applied Zeeman field in the momentum

*donghuixu@hubu.edu.cn

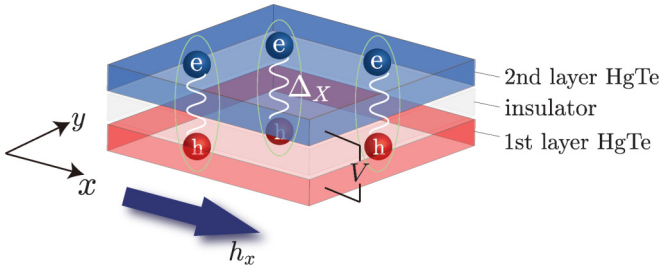

FIG. 1. Schematic illustration of the two coupled HgTe quantum wells with gating (electric bias V) under the applied in-plane Zeeman field h_x. Electrons and holes (marked by blue and red spheres) residing on two opposing layers are spatially separated by an insulator layer. The excitonic gap Δ_X couples electrons with holes to form an excitonic insulator through the interlayer Coulomb interaction.

space is given by

$$H_{\rm QSH}(\mathbf{k}) = M(\mathbf{k})\sigma_z + A(k_x\sigma_x s_z + k_y\sigma_y) - \frac{V}{2}\tau_z + \mathbf{h}\cdot\mathbf{s}, \qquad (1)$$

where the basis is $c^\dagger_{\mathbf{k}l} = (c^\dagger_{\mathbf{k}l\alpha\uparrow}, c^\dagger_{\mathbf{k}l\alpha\downarrow}, c^\dagger_{\mathbf{k}l\beta\uparrow}, c^\dagger_{\mathbf{k}l\beta\downarrow})$, α and β are different orbital degrees of freedom with opposite parity, $\uparrow$ and $\downarrow$ represent electron spin, and $l = 1, 2$ is the layer index. $s_{x,y,z}$, $\sigma_{x,y,z}$, and $\tau_{x,y,z}$ are the Pauli matrices acting on the spin, orbital, and layer degrees of freedom, respectively. τ_0, σ_0, and s_0 are the 2×2 identity matrices. $M(\mathbf{k}) = M - B(k_x^2 + k_y^2)$, where the Dirac mass parameter M determines the topological insulator phase, and V is the bias potential. $\mathbf{h}$ denotes the applied in-plane Zeeman field. When $V = 0$, this Hamiltonian is exactly two copies of the Bernevig-Hughes-Zhang (BHZ) model [96] that describes the HgTe/CdTe quantum wells. The topologically nontrivial phase of the BHZ model on a square lattice exits when $0 < M/(2B/a^2) < 2$ with the lattice constant a. We have assumed the spatial separation between these two layers to be sufficiently large so that the single-particle tunneling between layers can be neglected. Note that the model parameters are dependent on the thickness of the quantum wells. In subsequent calculations, the following parameters remain unchanged, $A = 275$ meV nm, $B = -1300$ meV nm^2, and the lattice constant is $a = 20$ nm [23]. The results remain valid when the parameters vary. For our purpose, we set the Dirac mass $M = -3$ meV in this section. In this case, each layer has inverted bands and contributes a Kramers pair of helical gapless edge states as shown in Fig. 2(a).

By turning on the electric bias V, an electron Fermi surface and a hole Fermi surface are created on layer 1 and layer 2, respectively. Coherent exciton condensation can be induced by the interlayer Coulomb interaction. Throughout this paper, we focus on the time-reversal invariant s-wave exciton pairings which should be the leading order from the mean-field decomposition of the screened interlayer Coulomb interaction. In general, the s-wave excitonic order parameters could provide an energy gain to the system, which can be expressed as $H_X = \Delta_X \tau_i \sigma_j s_k$ with $\Delta_X > 0$ the pairing strength (the sign change in Δ_X does not affect the following results) and the subscripts $i, j, k = 0, x, y, z$. The excitonic order parameters are considered to be momentum independent thanks to the short-range interaction. There are four relevant interlayer excitonic order parameters preserving time-reversal symmetry,

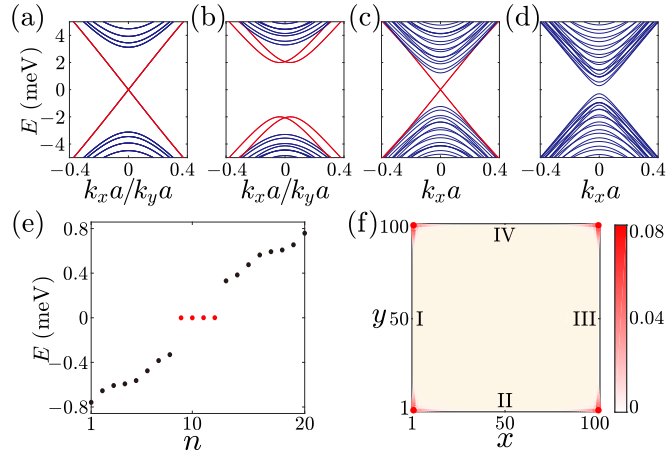

FIG. 2. Band structure of a ribbon geometry for (a) $V = \Delta_X = h_x = 0$, (b) $V = 1$ meV, $\Delta_X = 2$ meV, $h_x = 0$, (c) $V = 1$ meV, $\Delta_X = 2$ meV, $h_x = h_x^c \approx 2.06$ meV, and (d) $V = 1$ meV, $\Delta_X = 2$ meV, $h_x = 3$ meV. In (a) and (b), open boundary conditions along the x direction or y direction give rise to the same results. We take the open boundary condition in the y direction for (c) and (d). The edge states marked by solid red lines are merged with the 2D bulk in (d). (e) Energy spectrum of an $L_x \times L_y = 100\times100$ square-shaped sample exhibiting four midgap corner states marked by the red dots. We use the same parameter values as in (d). (f) Probability distribution of corner states indicated in energy spectrum in (e).

which are proportional to $\tau_x\sigma_z s_0$, $\tau_y\sigma_z s_z$, $\tau_y\sigma_x s_x$, and $\tau_y\sigma_x s_y$ [23]. We present more details of these four excitonic order parameters in Ref. [97]. Among these order parameters, it was found that the $\tau_x\sigma_z s_0$-type and $\tau_y\sigma_z s_z$-type orders can open a topological energy gap in the semimetallic bilayer HgTe/CdTe quantum wells, i.e., $M = 0$, resulting in a helical topological excitonic insulator characterized by the $\mathbb{Z}_2$ topological invariant, while the $\tau_y\sigma_x s_x$-type and $\tau_y\sigma_x s_y$-type pairings only lead to a topologically trivial energy gap in the case of $M = 0$ [23].

Next, we consider the case of $M < 0$ with the $\tau_y\sigma_x s_x$-type interlayer excitonic order. The $\tau_y\sigma_x s_y$-type order will give rise to the similar results, which is not discussed here. In the presence of the $\tau_y\sigma_x s_x$-type order, the two pairs of helical edge states are not stable and gapped out as depicted in Fig. 2(b). When an in-plane Zeeman field h_x is applied along the x direction, we can see that the quasiparticle edge gap along the k_x direction closes at the critical field h_x^c as shown in Fig. 2(c) and reopens as h_x increases [see Fig. 2(d)]. Whereas, during this process, we verified that the edge gap along the k_y direction does not show the closing-and-reopening behavior but only has a slight change in its amplitude. When $h_x > h_x^c$, two distinct types of edge gaps are formed along the x and y directions, then we calculate the energy spectrum for a finite-sized square sample as shown in Fig. 2(e). We observe four zero-energy boundary-obstructed midgap states, which are located at the four corners of the square sample by measuring the probability density [as shown in Fig. 2(f)].

Next, we discuss the above observed midgap states that are actually the topologically protected ECs. To unveil their topological property, we calculate the edge polarization by using the Wilson loop operators [38,41,50]. For a ribbon geometry with N_y unit cells in the y direction and $N_{\rm orb}$

degrees of freedom per unit cell, we express the Wilson loop operator W_{x,k_x} on a path along the k_x direction as $W_{x,k_x} = F_{x,k_x+(N_x-1)\Delta k_x} \cdots F_{x,k_x+\Delta k_x} F_{x,k_x}$, where $[F_{x,k_x}]^{mn} = \langle u^m_{k_x+\Delta k_x} | u^n_{k_x} \rangle$ with the step $\Delta k_x = 2\pi/N_x$, and $|u^n_{k_x}\rangle$ denotes the occupied Bloch functions with $n = 1, \ldots, N_{\rm occ}$. $N_{\rm occ} = N_{\rm orb}N_y/2$ is the number of occupied bands. The Wilson loop operator W_{x,k_x} satisfies the following eigenvalue equation

$$W_{x,k_x} \left|\nu^j_{x,k_x}\right\rangle = e^{i2\pi\nu^j_x} \left|\nu^j_{x,k_x}\right\rangle, \tag{2}$$

where $j = 1, \ldots N_{\rm occ}$. We can define the Wannier Hamiltonian $H_{W_x}(k_x)$ as $W_{x,k_x} \equiv e^{iH_{W_x}(k_x)}$, of which the eigenvalues $2\pi\nu_x$ correspond to the Wannier spectrum. The tangential polarization as a function of R_y is given as [38,41,50]

$$p_x(R_y) = \sum_{j=1}^{N_{\rm occ}\times N_y} \rho^j(R_y)\nu^j_x, \tag{3}$$

where $\rho^j(R_y) = \frac{1}{N_x}\sum_{k_x,\alpha,n} |[u^n_{k_x}]^{R_y,\alpha}[\nu^j_{k_x}]^n|^2$ is the probability density. $[u^n_{k_x}]^{R_y,\alpha}$ with $\alpha = 1, \ldots, N_{\rm orb}$, $R_y = 1, \ldots, N_y$ represents the components of the occupied states, and $[\nu^j_{x,k_x}]^n$ is the nth component of $|\nu^j_{x,k_x}\rangle$. The edge polarization at the y-normal edge is defined by $p_x^{{\rm edge},y} = \sum_{R_y=1}^{N_y/2} p_x(R_y)$. To fix the sign of the polarization, we add a perturbation term $\delta\tau_y\sigma_x s_y$ in our calculations. Similarly, we can derive ν_y and $p_y^{{\rm edge},x}$. We plot the Wannier spectra ν_x and ν_y as a function of h_x in Figs. 3(a) and 3(b), respectively. When the in-plane Zeeman field is greater than the critical field h_x^c, the ECs appear. Correspondingly, the Wannier spectrum ν_x has a pair of values pinned at 1/2, resulting in half quantized edge polarization $p_x^{{\rm edge},y}$ shown in Fig. 3(c). In contrast, $p_y^{{\rm edge},x}$ remains vanishing even for $h_x > h_x^c$. It indicates that the ECs originate from the quantized edge polarization $p_x^{{\rm edge},y}$.

Edge theory. To provide an intuitive picture to the appearance of ECs, we construct the edge theory [64] to analyze the topological mass on each edge. For simplicity, we focus on the $V = 0$ case since the bias has no contribution to the formation of edge mass. The low-energy Hamiltonian of the exciton condensate around the Γ point reads

$$H(\mathbf{k}) = A(k_x\sigma_x s_z + k_y\sigma_y) + \left[M - B\left(k_x^2 + k_y^2\right)\right]\sigma_z + \Delta_X\tau_y\sigma_x s_x + h_x s_x. \tag{4}$$

We first consider a semi-infinite geometry occupying the space $x \geqslant 0$ for edge I as marked in Fig. 2(f). In the spirit of $\mathbf{k}\cdot\mathbf{p}$ theory, we replace $k_x \to -i\partial_x$ and divide the Hamiltonian into $H = H_0(-i\partial_x) + H_p(k_y)$, in which

$$H_0(-i\partial_x) = -iA\sigma_x s_z\partial_x + \left(M + B\partial_x^2\right)\sigma_z,$$
$$H_p(k_y) = Ak_y\sigma_y + \Delta_X\tau_y\sigma_x s_x, \tag{5}$$

where all the k_y^2 terms have been omitted, and $h_x = 0$ for edge I. So we can solve H_0 first, and regard H_p as a perturbation, which is justified when the exciton gap is small compared to the energy gap. The eigenvalue equation $H_0\psi_\alpha(x) = E_\alpha\psi_\alpha(x)$ can be solved under the boundary condition $\psi_\alpha(0) = \psi_\alpha(+\infty) = 0$. A straightforward calculation gives four degenerate solutions with $E_\alpha = 0$, whose eigenstates can be written

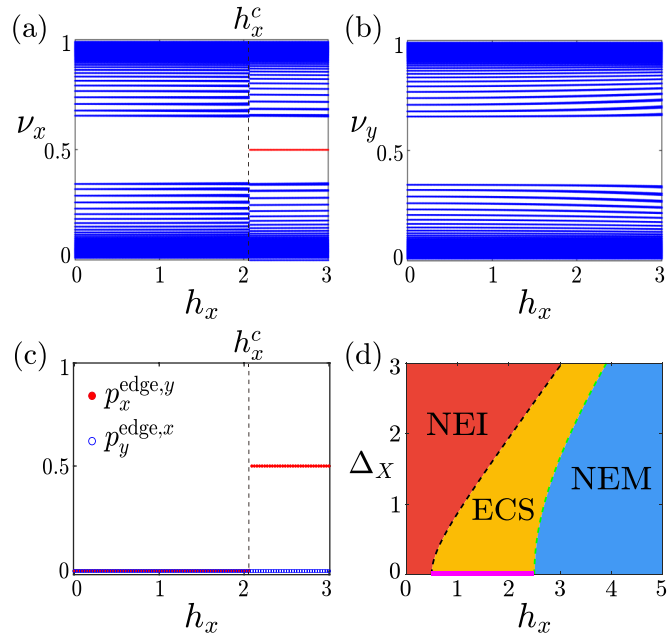

FIG. 3. (a), (b) Wannier spectra ν_x and ν_y versus h_x. (c) Edge polarization $p_x^{{\rm edge},y}$ and $p_y^{{\rm edge},x}$ along y-normal and x-normal edges, respectively. In (a)–(c), $V = 1$ meV and $\Delta_X = 2$ meV are used. (d) Phase diagram for topological ECs in the $\tau_y\sigma_x s_x$-type exciton condensation on the plane formed by Δ_X and h_x. The red color region marked by NEI stands for the normal excitonic insulator, the orange region marked by ECS denotes the region that supports topological ECs, and the blue region means a normal excitonic metal. For $\Delta_X = 0$ and $h_x > |V|/2$, the edge states are gapped along the x direction but remain gapless along the y direction, which is marked by the solid magenta line. The dashed lines are phase boundaries determined by the topological condition for ECs $\frac{1}{2}\sqrt{|V|^2 + 4\Delta_X^2} < h_x < \frac{1}{2}\sqrt{(2M + |V|)^2 + 4\Delta_X^2}$ (see Ref. [97] for the details of the derivations of phase boundary conditions), which agree well with the numerical results.

in the following form

$$\psi_\alpha(x) = N_x \sin(\kappa_1 x)e^{-\kappa_2 x}e^{ik_y y}\chi_\alpha, \tag{6}$$

where $\alpha = 1, \ldots 4$, and the normalization constant $N_x = 2\sqrt{\kappa_2(\kappa_1^2 + \kappa_2^2)/\kappa_1}$ with $\kappa_1 = \sqrt{(4BM - A^2)/4B^2}$ and $\kappa_2 = -A/2B$. The eigenvectors χ_α are determined by $\sigma_y s_z\chi_\alpha = -\chi_\alpha$. Here we choose

$$\chi_1 = |\sigma_y = -1\rangle \otimes |\uparrow\rangle \otimes |\tau_z = +1\rangle,$$
$$\chi_2 = |\sigma_y = +1\rangle \otimes |\downarrow\rangle \otimes |\tau_z = +1\rangle,$$
$$\chi_3 = |\sigma_y = -1\rangle \otimes |\uparrow\rangle \otimes |\tau_z = -1\rangle,$$
$$\chi_4 = |\sigma_y = +1\rangle \otimes |\downarrow\rangle \otimes |\tau_z = -1\rangle. \tag{7}$$

In this basis set, the matrix elements of the perturbation $H_p(k_y)$ are represented as

$$H_{{\rm I},\alpha\beta}(k_y) = \int_0^{+\infty} dx\psi^\dagger_\alpha(x)H_p(k_y)\psi_\beta(x), \tag{8}$$

which can be written in a more compact form

$$H_{\rm I} = -Ak_y s_z - \Delta_X\tau_y s_y. \tag{9}$$

Similarly, for edges II, III, and IV, we obtain

$$\begin{aligned} H_{\mathrm{II}} &= -Ak_x s_z - \Delta_X \tau_y s_x + h_x s_x, \\ H_{\mathrm{III}} &= Ak_y s_z - \Delta_X \tau_y s_y, \\ H_{\mathrm{IV}} &= Ak_x s_z - \Delta_X \tau_y s_x + h_x s_x. \end{aligned} \tag{10}$$

To be more clear, we introduce a unitary transformation $U = \frac{1}{\sqrt{2}}\begin{pmatrix} i & -i \\ 1 & 1 \end{pmatrix}$, then the edge Hamiltonians become

$$\begin{aligned} \widetilde{H}_{\mathrm{I}} &= -Ak_y s_z + \Delta_X \tau_z s_y, \\ \widetilde{H}_{\mathrm{II}} &= -Ak_x s_z + \Delta_X \tau_z s_x + h_x s_x, \\ \widetilde{H}_{\mathrm{III}} &= Ak_y s_z + \Delta_X \tau_z s_y, \\ \widetilde{H}_{\mathrm{IV}} &= Ak_x s_z + \Delta_X \tau_z s_x + h_x s_x. \end{aligned} \tag{11}$$

Now all the edge Hamiltonians are block diagonal. The effective masses of edges I and III are $M_{\mathrm{I}} = M_{\mathrm{III}} = \Delta_X$, while the effective masses of edges II and IV in the two blocks are $M_{\mathrm{II}} = M_{\mathrm{IV}} = \Delta_X + h_x, \Delta_X - h_x$. Therefore, $h_x > \Delta_X$ is the topological criteria to realize the topological ECs when $V = 0$. Consequently, the effective edge masses of two adjacent boundaries have different sign, so mass domain walls appear at the intersection of these boundaries, which results in zero-energy excitonic modes according to the Jackiw-Rebbi theory [98].

In Fig. 3(d), we present the phase diagram of the bilayer system with the $\tau_y\sigma_x s_x$-type exciton condensate which is subjected to the in-plane Zeeman field h_x. The topological excitonic corner state phase (ECS) occupies the regime between the normal excitonic insulator phase (NEI) and the normal excitonic metal phase (NEM). Here, the phase boundaries can be determined by the gap closing of the bulk at $h_x = \frac{1}{2}\sqrt{|V|^2 + 4\Delta_X^2}$ and $h_x = \frac{1}{2}\sqrt{(2M + |V|)^2 + 4\Delta_X^2}$, which agree well with the numerical results. The topological region becomes narrower by increasing the voltage V. Therefore, the topological ECs, characterized by the quantized edge polarization, can be realized by tuning the gate and in-plane Zeeman field.

It is necessary to point out that the in-plane Zeeman field along the y direction cannot induce topological ECs in the case of $\tau_y\sigma_x s_x$-type exciton condensate. We give a more detailed explanation in Ref. [97] based on the edge theory.

Excitonic corner states and nodal phase for the positive Dirac mass. Next, we discuss if we can still realize the topological ECs in the bilayer system without band inversion occurring in each layer. For the $\tau_x\sigma_z s_0$-type exciton condensate, the in-plane Zeeman field can also generate ECs even when H_{QSH} has non-negative mass $M \geqslant 0$. For our purpose, we set $M = 3$ meV in this section. Note that the bilayer system is a topologically trivial semiconductor in the absence of excitonic orders. The numerical calculation shows the in-plane Zeeman field h_x induces two ECs located at the left and right corners for a diamond-shaped sample [see Fig. 4(a)].

Although the Zeeman field breaks time-reversal symmetry, h_x preserves the twofold rotation symmetry about the x axis $C_{2x} = i\sigma_z s_x$. The first Brillouin zone has a mirror-invariant line $k_y = 0$ preserving the C_{2x} symmetry. We can adopt the mirror winding number [99] along this line to characterize the topological properties of this type of ECs. In this line,

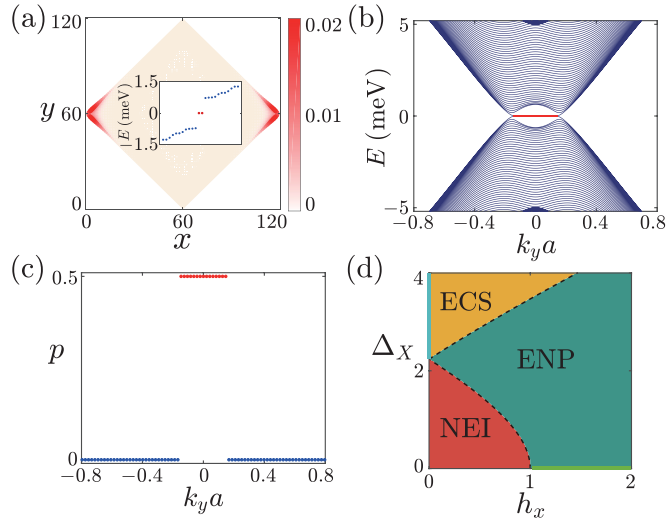

FIG. 4. (a) Probability distribution of ECs. Inset: energy spectrum. (b) Energy dispersion of the nodal phase for a ribbon geometry with open boundary condition along the x direction. (c) Bulk polarization of the nodal phase as a function of k_y. (d) Phase diagram of $\tau_x\sigma_z s_0$-type exciton condensation under the in-plane Zeeman field. The bottle green regime marked by ENP represents the excitonic nodal phase. Same as in Fig. 2(d), the red color region marked by NEI stands for the normal excitonic insulator, and the orange region marked by ECS denotes the excitonic corner state phase. The solid green line means the normal metal driven by h_x when $\Delta_X = 0$, while the solid cyan line denotes the helical excitonic insulator induced by the $\tau_x\sigma_z s_0$-type pairing when $h_x = 0$. In (a), (b), and (c), we set $V =$ 4 meV, $\Delta_X = 5$ meV, $h_x = 3$ meV for (b) and (c), and $h_x = 1$ meV for (a). In all plots, we choose $M = 3$ meV.

$H(k_x, k_y = 0)$ is invariant under the operation of C_{2x}. The discrete version of $H(k_x, 0)$ has the following form

$$\begin{aligned} H(k_x, 0) = &\frac{A}{a}\sin(k_x a)\sigma_x s_z + M(k_x, 0)\sigma_z \\ &+ h_x s_x - \frac{V}{2}\tau_z + \Delta_X \tau_x \sigma_z, \end{aligned} \tag{12}$$

where $M(k_x, 0) = M - B[2 - 2\cos(k_x a)]/a^2$. C_{2x} has two fourfold degenerate eigenvalues of ± 1, the eigenvectors of ± 1 are $1/\sqrt{2}|\alpha\rangle \otimes (|\downarrow\rangle \pm |\uparrow\rangle) \otimes |l = 2\rangle$, $1/\sqrt{2}|\beta\rangle \otimes (|\downarrow\rangle \mp |\uparrow\rangle) \otimes |l = 2\rangle$, $1/\sqrt{2}|\alpha\rangle \otimes (|\downarrow\rangle \pm |\uparrow\rangle) \otimes |l = 1\rangle$, $1/\sqrt{2}|\beta\rangle \otimes (|\downarrow\rangle \mp |\uparrow\rangle) \otimes |l = 1\rangle$, where $|\alpha\rangle(|\beta\rangle)$, $|\uparrow\rangle(|\downarrow\rangle)$, and $|l = 1, 2\rangle(|2\rangle)$ are the basis vectors acting on the orbit, spin, and layer subspaces, respectively. Due to the conserving of C_{2x}, we project $H(k_x, 0)$ into the two subspaces corresponding to $C_{2x} = \pm 1$, i.e., $H(k_x, 0) = H_+(k_x, 0) \oplus H_-(k_x, 0)$. The block Hamiltonians read

$$\begin{aligned} H_\pm(k_x, 0) = &[M(k_x, 0) \pm h_x]\sigma_z - \frac{V}{2}\tau_z \\ &- \frac{A}{a}\sin(k_x a)\sigma_x + \Delta_X \tau_x \sigma_z. \end{aligned} \tag{13}$$

Along the line $k_y = 0$, we consider the Wilson loop operator $W_{\pm,k_x}$, then the mirror winding number $\nu_\pm$ can be evaluated by [99]

$$\nu_\pm = \frac{1}{i\pi}\log(\det[W_{\pm,k_x}]) \bmod 2. \tag{14}$$

When the ECs emerge, the mirror winding number shows that $\nu_+ = \nu_- = 1$.

Now let us discuss the excitonic order induced nodal phase in the bilayer system. In the case of the $\tau_x\sigma_z s_0$-type exciton pairing, a nodal phase with Weyl nodes along the k_y axis emerges. The excitonic nodal phase hosts flat band edge states as shown in Fig. 4(b). In order to characterize the topological properties of nodal phase, we use the Wilson loop method to calculate the bulk polarization of the system. By treating k_y as a parameter, the Hamiltonian is effectively reduced to a one-dimensional Hamiltonian $H_{k_y}(k_x)$. For fixed k_y, considering the Wilson loop operator in the x direction W_{x,k_x}, the Wannier center ν_x^j is obtained by the following equation

$$W_{x,k_x}\left|\nu_{x,k_x}^j\right\rangle = e^{i2\pi\nu_x^j}\left|\nu_{x,k_x}^j\right\rangle. \tag{15}$$

Then, the bulk polarization can be defined as $p = \sum_j \nu_x^j \bmod 1$ for a given k_y. In Fig. 4(c), we plot the calculated bulk polarization as a function of k_y. We can see that the polarization is quantized to $1/2$ between two nodes and vanishes at other k_y. Therefore, the topology of the nodal phase can be captured by the k_y-dependent polarization.

Finally, the phase diagram for $\tau_x\sigma_z s_0$-type exciton condensate on the plane of Δ_X and h_x is shown in Fig. 4(d). By numerically observing the gap closing of the bulk, we define the phase boundaries. Analytically, the boundary between the ECS and the excitonic nodal phase (ENP) is determined by $h_x = -M + \sqrt{\Delta_X^2 + |V|^2/4}$, while the boundary between the NEI and ENP is defined by $h_x = M - \sqrt{\Delta_X^2 + |V|^2/4}$ [97].

Conclusion and discussion. In this work, we identified two distinct types of ECs in the gated bilayer quantum spin Hall insulator model with s-wave exciton pairings in the presence of the in-plane Zeeman field. Experimentally, the ECs can be detected by scanning tunneling microscope measurements. ECs manifest themselves as in-plane Zeeman field dependent zero-bias peaks in differential conductance (see Sec. V in Ref. [97] for more details). The different patterns of the two types of ECs, in turn, could be used to determine the excitonic pairing of the excitonic insulator in experiments. We also found an excitonic nodal phase with the flat-band edge states in this system. Considering these exotic topological phases, our work will stimulate more investigations on higher-order topology and topological nodal phases in exciton condensates.

Different from superconducting pairings, excitonic pairings do not have to possess particle-hole symmetry. Therefore, ECs can appear at the finite energy, which is in contrast to Majorana corner states. In this paper, the ECs are pinned to zero energy as we use a particle-hole symmetric model. Removing particle-hole symmetry, we can still expect midgap ECs, but they will be shifted to the finite energy.

Additionally, we mainly focus on the corner states created in the time-reversal invariant singlet s-wave exciton condensates hereinbefore. In this case, an in-plane Zeeman field is necessary to create the ECs, whereas we would like to point out that Kramers pairs of ECs could be generated in this bilayer system without applying a Zeeman field when time-reversal invariant d-wave exciton pairings are formed.

Acknowledgments. D.-H.X. was supported by the NSFC (under Grants No. 12074108 and No. 11704106). B.Z. was supported by the NSFC (under Grant No. 12074107) and the program of outstanding young and middle-aged scientific and technological innovation team of colleges and universities in Hubei Province (under Grant No. T2020001). C.-Z.C. was funded by the NSFC (under Grant No. 11974256), the NSF of Jiangsu Province (under Grant No. BK20190813) and the Priority Academic Program Development (PAPD) of Jiangsu Higher Education Institution. D.-H.X. also acknowledges the financial support of the Chutian Scholars Program in Hubei Province.

[1] N. F. Mott, The transition to the metallic state, Philos. Mag. **6**, 287 (1961).

[2] R. S. Knox, Theory of excitons, Solid State Phys. Suppl. **5**, 100 (1963).

[3] L. V. K. Keldysh and Y. V. Kopaev, Possible instability of the semimetallic state toward Coulomb interaction, Fiz. Tverd. Tela **6**, 2791 (1964) [Sov. Phys. Solid State **6**, 2219 (1965)].

[4] D. Jérome, T. M. Rice, and W. Kohn, Excitonic insulator, Phys. Rev. **158**, 462 (1967).

[5] M. M. Fogler, L. V. Butov, and K. S. Novoselov, High-temperature superfluidity with indirect excitons in van der Waals heterostructures, Nat. Commun. **5**, 4555 (2014).

[6] J. I. A. Li, T. Taniguchi, K. Watanabe, J. Hone, and C. R. Dean, Excitonic superfluid phase in double bilayer graphene, Nat. Phys. **13**, 751 (2017).

[7] X. Liu, K. Watanabe, T. Taniguchi, B. I. Halperin, and P. Kim, Quantum Hall drag of exciton condensate in graphene, Nat. Phys. **13**, 746 (2017).

[8] Y. F. Lu, H. Kono, T. I. Larkin, A. W. Rost, T. Takayama, A. V. Boris, B. Keimer, and H. Takagi, Zero-gap semiconductor to excitonic insulator transition in Ta_2NiSe_5, Nat. Commun. **8**, 14408 (2017).

[9] D. Werdehausen, T. Takayama, M. Höppner, G. Albrecht, A. W. Rost, Y. Lu, D. Manske, H. Takagi, and S. Kaiser, Coherent order parameter oscillations in the ground state of the excitonic insulator Ta_2NiSe_5, Sci. Adv. **4**, eaap8652 (2018).

[10] Y. Wakisaka, T. Sudayama, K. Takubo, T. Mizokawa, M. Arita, H. Namatame, M. Taniguchi, N. Katayama, M. Nohara, and H. Takagi, Excitonic Insulator State in Ta_2 $NiSe_5$ Probed by Photoemission Spectroscopy, Phys. Rev. Lett. **103**, 026402 (2009).

[11] T. Kaneko, T. Toriyama, T. Konishi, and Y. Ohta, Orthorhombic-to-monoclinic phase transition of Ta_2 $NiSe_5$ induced by the Bose-Einstein condensation of excitons, Phys. Rev. B **87**, 035121 (2013).

[12] K. Sugimoto, S. Nishimoto, T. Kaneko, and Y. Ohta, Strong Coupling Nature of the Excitonic Insulator State in Ta_2 $NiSe_5$, Phys. Rev. Lett. **120**, 247602 (2018).

[13] G. Mazza, M. Rösner, L. Windgätter, S. Latini, H. Hübener, A. J. Millis, A. Rubio, and A. Georges, Nature of Symmetry

Breaking at the Excitonic Insulator Transition: Ta_2 $NiSe_5$, Phys. Rev. Lett. **124**, 197601 (2020).

[14] A. Kogar, M. S. Rak, S. Vig, A. A. Husain, F. Flicker, Y. I. Joe, L. Venema, G. J. MacDougall, T. C. Chiang, E. Fradkin, J. van Wezel, and P. Abbamonte, Signatures of exciton condensation in a transition metal dichalcogenide, Science **358**, 1314 (2017).

[15] H. Cercellier, C. Monney, F. Clerc, C. Battaglia, L. Despont, M. G. Garnier, H. Beck, P. Aebi, L. Patthey, H. Berger, and L. Forró, Evidence for an Excitonic Insulator Phase in 1T-$TiSe_2$, Phys. Rev. Lett. **99**, 146403 (2007).

[16] T. Kaneko, Y. Ohta, and S. Yunoki, Exciton-phonon cooperative mechanism of the triple-q charge-density-wave and antiferroelectric electron polarization in $TiSe_2$, Phys. Rev. B **97**, 155131 (2018).

[17] C. Chen, B. Singh, H. Lin, and V. M. Pereira, Reproduction of the Charge Density Wave Phase Diagram in 1T-$TiSe_2$ Exposes its Excitonic Character, Phys. Rev. Lett. **121**, 226602 (2018).

[18] B. Seradjeh, J. E. Moore, and M. Franz, Exciton Condensation and Charge Fractionalization in a Topological Insulator Film, Phys. Rev. Lett. **103**, 066402 (2009).

[19] N. Hao, P. Zhang, and Y. Wang, Topological phases and fractional excitations of the exciton condensate in a special class of bilayer systems, Phys. Rev. B **84**, 155447 (2011).

[20] G. Y. Cho and J. E. Moore, Quantum phase transition and fractional excitations in a topological insulator thin film with Zeeman and excitonic masses, Phys. Rev. B **84**, 165101 (2011).

[21] D. Tilahun, B. Lee, E. M. Hankiewicz, and A. H. MacDonald, Quantum Hall Superfluids in Topological Insulator Thin Films, Phys. Rev. Lett. **107**, 246401 (2011).

[22] D. K. Efimkin, Yu. E. Lozovik, and A. A. Sokolik, Electron-hole pairing in a topological insulator thin film, Phys. Rev. B **86**, 115436 (2012).

[23] J. C. Budich, B. Trauzettel, and P. Michetti, Time Reversal Symmetric Topological Exciton Condensate in Bilayer HgTe Quantum Wells, Phys. Rev. Lett. **112**, 146405 (2014).

[24] D. I. Pikulin and T. Hyart, Interplay of Exciton Condensation and the Quantum Spin Hall Effect in InAs/GaSb Bilayers, Phys. Rev. Lett. **112**, 176403 (2014).

[25] K. Chen and R. Shindou, Chiral topological excitons in a Chern band insulator, Phys. Rev. B **96**, 161101(R) (2017).

[26] Y. Hu, J. W. F. Venderbos, and C. L. Kane, Fractional Excitonic Insulator, Phys. Rev. Lett. **121**, 126601 (2018).

[27] Q. Zhu, M. W.-Y. Tu, Q. Tong, and W. Yao, Gate tuning from exciton superfluid to quantum anomalous Hall in van der Waals heterobilayer, Sci. Adv. **5**, eaau6120 (2019).

[28] L.-H. Hu, R.-X. Zhang, F.-C. Zhang, and C. Wu, Interacting topological mirror excitonic insulator in one dimension, Phys. Rev. B **102**, 235115 (2020).

[29] R. Wang, O. Erten, B. Wang, and D. Y. Xing, Prediction of a topological $p+ip$ excitonic insulator with parity anomaly, Nat. Commun. **10**, 1 (2019).

[30] D. Varsano, M. Palummo, E. Molinari, and M. Rontani, A monolayer transition-metal dichalcogenide as a topological excitonic insulator, Nat. Nanotechnol. **15**, 367 (2020).

[31] A. Blason and M. Fabrizio, Exciton topology and condensation in a model quantum spin Hall insulator, Phys. Rev. B **102**, 035146 (2020).

[32] E. Perfetto and G. Stefanucci, Floquet Topological Phase of Nondriven p-Wave Nonequilibrium Excitonic Insulators, Phys. Rev. Lett. **125**, 106401 (2020).

[33] Z. Sun and A. J. Millis, Topological Charge Pumping in Excitonic Insulators, Phys. Rev. Lett. **126**, 027601 (2021).

[34] L. Du, X. Li, W. Lou, G. Sullivan, K. Chang, J. Kono, and R.-R. Du, Evidence for a topological excitonic insulator in InAs/GaSb bilayers, Nat. Commun. **8**, 1971 (2017).

[35] W. Yu, V. Clericò, C. H. Fuentevilla, X. Shi, Y. Jiang, D. Saha, W. K. Lou, K. Chang, D. H. Huang, G. Gumbs *et al.*, Anomalously large resistance at the charge neutrality point in a zero-gap InAs/GaSb bilayer, New J. Phys. **20**, 053062 (2018).

[36] F. Zhang, C. L. Kane, and E. J. Mele, Surface State Magnetization and Chiral Edge States on Topological Insulators, Phys. Rev. Lett. **110**, 046404 (2013).

[37] R.-J. Slager, L. Rademaker, J. Zaanen, and L. Balents, Impurity-bound states and green's function zeros as local signatures of topology, Phys. Rev. B **92**, 085126 (2015).

[38] W. A. Benalcazar, B. A. Bernevig, and T. L. Hughes, Quantized electric multipole insulators, Science **357**, 61 (2017).

[39] J. Langbehn, Y. Peng, L. Trifunovic, F. von Oppen, and P. W. Brouwer, Reflection-Symmetric Second-Order Topological Insulators and Superconductors, Phys. Rev. Lett. **119**, 246401 (2017).

[40] Z. Song, Z. Fang, and C. Fang, $(d-2)$-Dimensional Edge States of Rotation Symmetry Protected Topological States, Phys. Rev. Lett. **119**, 246402 (2017).

[41] W. A. Benalcazar, B. A. Bernevig, and T. L. Hughes, Electric multipole moments, topological multipole moment pumping, and chiral hinge states in crystalline insulators, Phys. Rev. B **96**, 245115 (2017).

[42] F. Schindler, A. M. Cook, M. G. Vergniory, Z. Wang, S. S. P. Parkin, B. A. Bernevig, and T. Neupert, Higher-order topological insulators, Sci. Adv. **4**, eaat0346 (2018).

[43] M. Ezawa, Higher-Order Topological Insulators and Semimetals on the Breathing Kagome and Pyrochlore Lattices, Phys. Rev. Lett. **120**, 026801 (2018).

[44] M. Ezawa, Topological Switch Between Second-Order Topological Insulators and Topological Crystalline Insulators, Phys. Rev. Lett. **121**, 116801 (2018).

[45] M. Geier, L. Trifunovic, M. Hoskam, and P. W. Brouwer, Second-order topological insulators and superconductors with an order-two crystalline symmetry, Phys. Rev. B **97**, 205135 (2018).

[46] E. Khalaf, Higher-order topological insulators and superconductors protected by inversion symmetry, Phys. Rev. B **97**, 205136 (2018).

[47] M. Ezawa, Strong and weak second-order topological insulators with hexagonal symmetry and $\mathbb{Z}_3$ index, Phys. Rev. B **97**, 241402(R) (2018).

[48] F. K. Kunst, G. van Miert, and E. J. Bergholtz, Lattice models with exactly solvable topological hinge and corner states, Phys. Rev. B **97**, 241405(R) (2018).

[49] G. van Miert and C. Ortix, Higher-order topological insulators protected by inversion and rotoinversion symmetries, Phys. Rev. B **98**, 081110(R) (2018).

[50] S. Franca, J. van den Brink, and I. C. Fulga, An anomalous higher-order topological insulator, Phys. Rev. B **98**, 201114(R) (2018).

[51] Y. You, T. Devakul, F. J. Burnell, and T. Neupert, Higher-order symmetry-protected topological states for interacting bosons and fermions, Phys. Rev. B **98**, 235102 (2018).

[52] S. H. Kooi, G. van Miert, and C. Ortix, Inversion-symmetry protected chiral hinge states in stacks of doped quantum Hall layers, Phys. Rev. B **98**, 245102 (2018).

[53] L. Trifunovic and P. W. Brouwer, Higher-Order Bulk-Boundary Correspondence for Topological Crystalline Phases, Phys. Rev. X **9**, 011012 (2019).

[54] F. Liu, H.-Y. Deng, and K. Wakabayashi, Helical Topological Edge States in a Quadrupole Phase, Phys. Rev. Lett. **122**, 086804 (2019).

[55] H. Fan, B. Xia, L. Tong, S. Zheng, and D. Yu, Elastic Higher-Order Topological Insulator with Topologically Protected Corner States, Phys. Rev. Lett. **122**, 204301 (2019).

[56] Z. Wang, B. J. Wieder, J. Li, B. Yan, and B. A. Bernevig, Higher-Order Topology, Monopole Nodal Lines, and the Origin of Large Fermi Arcs in Transition Metal Dichalcogenides XTe_2 (X= Mo,W), Phys. Rev. Lett. **123**, 186401 (2019).

[57] X.-L. Sheng, C. Chen, H. Liu, Z. Chen, Z.-M. Yu, Y. X. Zhao, and S. A. Yang, Two-Dimensional Second-Order Topological Insulator in Graphdiyne, Phys. Rev. Lett. **123**, 256402 (2019).

[58] R. Chen, C.-Z. Chen, J.-H. Gao, B. Zhou, and D.-H. Xu, Higher-Order Topological Insulators in Quasicrystals, Phys. Rev. Lett. **124**, 036803 (2020).

[59] D. Varjas, A. Lau, K. Pöyhönen, A. R. Akhmerov, D. I. Pikulin, and I. C. Fulga, Topological Phases Without Crystalline Counterparts, Phys. Rev. Lett. **123**, 196401 (2019).

[60] C.-B. Hua, R. Chen, B. Zhou, and D.-H. Xu, Higher-order topological insulator in a dodecagonal quasicrystal, Phys. Rev. B **102**, 241102(R) (2020).

[61] D. Călugăru, V. Juričić, and B. Roy, Higher-order topological phases: A general principle of construction, Phys. Rev. B **99**, 041301(R) (2019).

[62] W. A. Benalcazar, T. Li, and T. L. Hughes, Quantization of fractional corner charge in C_n-symmetric higher-order topological crystalline insulators, Phys. Rev. B **99**, 245151 (2019).

[63] M. Rodriguez-Vega, A. Kumar, and B. Seradjeh, Higher-order Floquet topological phases with corner and bulk bound states, Phys. Rev. B **100**, 085138 (2019).

[64] Z. Yan, F. Song, and Z. Wang, Majorana Corner Modes in a High-Temperature Platform, Phys. Rev. Lett. **121**, 096803 (2018).

[65] Q. Wang, C.-C. Liu, Y.-M. Lu, and F. Zhang, High-Temperature Majorana Corner States, Phys. Rev. Lett. **121**, 186801 (2018).

[66] X. Zhu, Tunable majorana corner states in a two-dimensional second-order topological superconductor induced by magnetic fields, Phys. Rev. B **97**, 205134 (2018).

[67] V. Dwivedi, C. Hickey, T. Eschmann, and S. Trebst, Majorana corner modes in a second-order Kitaev spin liquid, Phys. Rev. B **98**, 054432 (2018).

[68] Y. Wang, M. Lin, and T. L. Hughes, Weak-pairing higher order topological superconductors, Phys. Rev. B **98**, 165144 (2018).

[69] T. Liu, J. J. He, and F. Nori, Majorana corner states in a two-dimensional magnetic topological insulator on a high-temperature superconductor, Phys. Rev. B **98**, 245413 (2018).

[70] Y. Volpez, D. Loss, and J. Klinovaja, Second-Order Topological Superconductivity in π-Junction Rashba Layers, Phys. Rev. Lett. **122**, 126402 (2019).

[71] X.-H. Pan, K.-J. Yang, L. Chen, G. Xu, C.-X. Liu, and X. Liu, Lattice-Symmetry-Assisted Second-Order Topological Superconductors and Majorana Patterns, Phys. Rev. Lett. **123**, 156801 (2019).

[72] Z. Yan, Higher-Order Topological Odd-Parity Superconductors, Phys. Rev. Lett. **123**, 177001 (2019).

[73] Z. Yan, Majorana corner and hinge modes in second-order topological insulator/superconductor heterostructures, Phys. Rev. B **100**, 205406 (2019).

[74] S. Franca, D. V. Efremov, and I. C. Fulga, Phase-tunable second-order topological superconductor, Phys. Rev. B **100**, 075415 (2019).

[75] R.-X. Zhang, W. S. Cole, and S. Das Sarma, Helical Hinge Majorana Modes in Iron-Based Superconductors, Phys. Rev. Lett. **122**, 187001 (2019).

[76] R.-X. Zhang, W. S. Cole, X. Wu, and S. Das Sarma, Higher-Order Topology and Nodal Topological Superconductivity in Fe(Se,Te) Heterostructures, Phys. Rev. Lett. **123**, 167001 (2019).

[77] R.-X. Zhang, F. Wu, and S. Das Sarma, Möbius Insulator and Higher-Order Topology in $MnBi_{2n}$ Te_{3n+1}, Phys. Rev. Lett. **124**, 136407 (2020).

[78] C. Zeng, T. D. Stanescu, C. Zhang, V. W. Scarola, and S. Tewari, Majorana Corner Modes with Solitons in an Attractive Hubbard-Hofstadter Model of Cold Atom Optical Lattices, Phys. Rev. Lett. **123**, 060402 (2019).

[79] C. W. Peterson, W. A. Benalcazar, T. L. Hughes, and G. Bahl, A quantized microwave quadrupole insulator with topologically protected corner states, Nature (London) **555**, 346 (2018).

[80] H. Xue, Y. Yang, F. Gao, Y. Chong, and B. Zhang, Acoustic higher-order topological insulator on a kagome lattice, Nat. Mater. **18**, 108 (2018).

[81] X. Ni, M. Weiner, A. Alù, and A. B. Khanikaev, Observation of higher-order topological acoustic states protected by generalized chiral symmetry, Nat. Mater. **18**, 113 (2018).

[82] F. Schindler, Z. Wang, M. G. Vergniory, A. M. Cook, A. Murani, S. Sengupta, A. Y. Kasumov, R. Deblock, S. Jeon, I. Drozdov *et al.*, Higher-order topology in bismuth, Nat. Phys. **14**, 918 (2018).

[83] S. Imhof, C. Berger, F. Bayer, J. Brehm, L. W. Molenkamp, T. Kiessling, F. Schindler, C. H. Lee, M. Greiter, T. Neupert, and R. Thomale, Topolectrical-circuit realization of topological corner modes, Nat. Phys. **14**, 925 (2018).

[84] J. Noh, W. A. Benalcazar, S. Huang, M. J. Collins, K. P. Chen, T. L. Hughes, and M. C. Rechtsman, Topological protection of photonic mid-gap defect modes, Nat. Photon. **12**, 408 (2018).

[85] X. Zhang, H.-X. Wang, Z.-K. Lin, Y. Tian, B. Xie, M.-H. Lu, Y.-F. Chen, and J.-H. Jiang, Second-order topology and multidimensional topological transitions in sonic crystals, Nat. Phys. **15**, 582 (2019).

[86] S. N. Kempkes, M. R. Slot, J. J. van den Broeke, P. Capiod, W. A. Benalcazar, D. Vanmaekelbergh, D. Bercioux, I. Swart, and C. M. Smith, Robust zero-energy modes in an electronic higher-order topological insulator, Nat. Mater. **18**, 1292 (2019).

[87] S. Mittal, V. V. Orre, G. Zhu, M. A. Gorlach, A. Poddubny, and M. Hafezi, Photonic quadrupole topological phases, Nat. Photon. **13**, 692 (2019).

[88] A. E. Hassan, F. K. Kunst, A. Moritz, G. Andler, E. J. Bergholtz, and M. Bourennane, Corner states of light in photonic waveguides, Nat. Photon. **13**, 697 (2019).

[89] E. Lee, R. Kim, J. Ahn, and B.-J. Yang, Two-dimensional higher-order topology in monolayer graphdiyne, npj Quantum Mater. **5**, 1 (2020).

[90] K. Kudo, T. Yoshida, and Y. Hatsugai, Higher-Order Topological Mott Insulators, Phys. Rev. Lett. **123**, 196402 (2019).

[91] Y. Xu, Z. Song, Z. Wang, H. Weng, and X. Dai, Higher-Order Topology of the Axion Insulator $EuIn_2$ As_2, Phys. Rev. Lett. **122**, 256402 (2019).

[92] C. Yue, Y. Xu, Z. Song, H. Weng, Y.-M. Lu, C. Fang, and X. Dai, Symmetry-enforced chiral hinge states and surface quantum anomalous Hall effect in the magnetic axion insulator Bi_{2-x} Sm_x Se_3, Nat. Phys. **15**, 577 (2019).

[93] Y. Ren, Z. Qiao, and Q. Niu, Engineering Corner States from Two-Dimensional Topological Insulators, Phys. Rev. Lett. **124**, 166804 (2020).

[94] Y.-J. Wu, J. Hou, Y.-M. Li, X.-W. Luo, X. Shi, and C. Zhang, In-Plane Zeeman-Field-Induced Majorana Corner and Hinge Modes in an *s*-Wave Superconductor Heterostructure, Phys. Rev. Lett. **124**, 227001 (2020).

[95] G. M. Gusev, E. B. Olshanetsky, F. G. G. Hernandez, O. E. Raichev, N. N. Mikhailov, and S. A. Dvoretsky, Two-dimensional topological insulator state in double HgTe quantum well, Phys. Rev. B **101**, 241302 (2020).

[96] B. A. Bernevig, T. L. Hughes, and S.-C. Zhang, Quantum spin Hall effect and topological phase transition in HgTe quantum wells, Science **314**, 1757 (2006).

[97] See Supplemental Material at http://link.aps.org/supplemental/10.1103/PhysRevB.103.L201115 for more details of excitonic order parameters, the effect of different in-plane Zeeman field components, the derivations of phase boundary conditions, and local density of states plots.

[98] R. Jackiw and C. Rebbi, Solitons with fermion number 1/2, Phys. Rev. D **13**, 3398 (1976).

[99] M. J. Park, Y. Kim, G. Y. Cho, and SungBin Lee, Higher-Order Topological Insulator in Twisted Bilayer Graphene, Phys. Rev. Lett. **123**, 216803 (2019).